Proc IMechE Part A: Journal of Power and Energy

Steady Computations of Ingress through Gas Turbine Rim Seals

Yogesh Lalwani **Carl M Sangan** **Mike Wilson** **Gary D Lock**

Department of Mechanical Engineering,
University of Bath,
Bath, BA2 7AY,
United Kingdom

Corresponding author:
Carl M Sangan, Department of Mechanical Engineering, University of Bath, Bath, BA2 7AY, UK
Email: c.m.sangan@bath.ac.uk

Abstract

In gas turbines, rim seals are fitted at the periphery of the wheel-space between the turbine disc and its adjacent casing; their purpose is to reduce the ingress of hot mainstream gases. This paper describes the use of a three-dimensional (3D), steady-state model to investigate ingress through engine-representative single and double radial-clearance seals. The 3D Reynolds-Average Navier-Stokes (RANS) computations of a simplified turbine stage are carried out using the commercial computational fluid dynamics code ANSYS CFX v13, and the model is based on the geometry of an experimental test rig at the University of Bath. The measured variation of the peak-to-trough pressure difference in the annulus, which is the main driving mechanism for ingress, is reproduced well qualitatively by the computations; quantitatively, the maximum local differences between computation and experiment are less than 20% of the measured peak-to-trough circumferential variation. The radial variation of swirl ratio in the rotor-stator wheel-space is well predicted over the range of flow rates and rim-seal geometries studied. The radial distribution of sealing effectiveness determined from experiments is reproduced inward of the mixing region near the seal clearance over a range of sealing flow rates; some over-prediction of the effectiveness was found for both seals at high radius, probably due to limitations in the turbulent mixing modelling.

The 3D steady-state approach may be a practical tool for the engine designer where there is a lack of experimental data, providing quantitative predictions of the flow structure within the rotor-stator wheel-space and qualitative predictions of the sealing effectiveness for a given rim-seal geometry.

Keywords

Gas turbine cooling, Internal air systems, Computational fluid dynamics

Introduction

A typical high-pressure gas-turbine stage is depicted in Figure 1(a). Cooling of the turbine components allows the mainstream gas temperature to exceed the blade and vane material melting point without affecting the integrity of these components. It is important to prevent the ingress of hot mainstream gas into the wheel-space between the stator and rotating disc; this is achieved by supplying the required quantity of cooling and sealing air, which flows outwards over the disc face. The flow is usually controlled by an inner seal (not shown in Figure 1) and is expelled from the wheel-space into the mainstream gas path through the rim seal. Although the sealing air can reduce ingress, superfluous use reduces the engine efficiency and insufficient flow can cause serious overheating, resulting in damage to the turbine rim and blade roots. Rim seals, such as that shown in Figure 1 (b) are fitted at the periphery of the wheel-space to limit ingress.

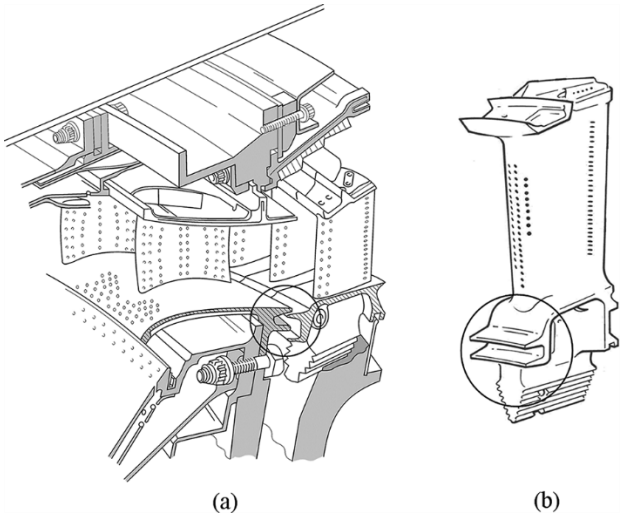

Figure 1: (a) Typical high-pressure gas-turbine stage; (b) Detail of rim seal[1]

The flow past the stationary vanes and rotating blades in the turbine annulus creates an unsteady 3D variation of pressure radially outward of the rim seal, as depicted in Figure 2. Ingress and egress occurs through those parts of the seal clearance where the external pressure is higher and lower, respectively, than that in the wheel-space; this non-axisymmetric type of ingress is referred to as *externally-induced* (EI) ingress. In gas turbines, EI ingress is dominant. Engine designers often use double rim seals (such as that shown in Figure 2) where the circumferential variation in pressure is attenuated in the *outer wheel-space* between the two seals.

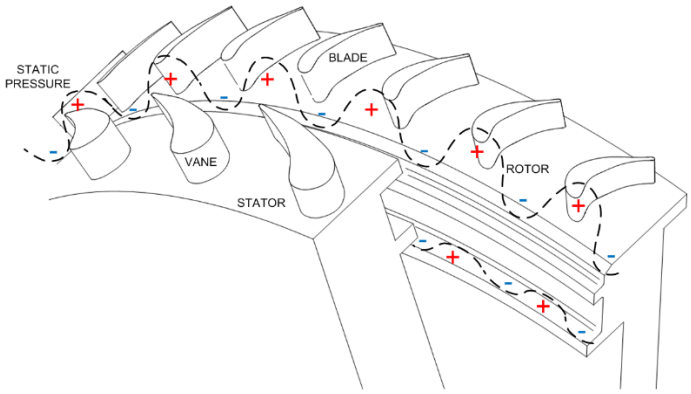

Figure 2: Typical pressure asymmetry in the annulus and outer wheel-space for a double seal

Figure 3 is a simplified, axisymmetric diagram of the fluid mechanics of ingress and egress through an axial-clearance rim seal. The flow structure in a typical rotating-disc system is governed by λ_T, the turbulent flow parameter, and depends weakly on Re_ϕ, the rotational Reynolds number[2,3]. A value of $\lambda_T = 0.22$ is associated with the flow-rate entrained by a free disc, and values above this level are expected to suppress the core rotation (with swirl ratio β) in the wheel-space. In Figure 3, where $\lambda_T << 0.22$, there are separate boundary layers on the rotating and stationary discs with a rotating core of inviscid fluid between the boundary layers. The superposed sealing flow enters the system through an inner region and is entrained into the boundary layer on the rotor. In the outer region, where the ingress and egress mix, fluid leaves the system through the rim seal; conservation of mass, angular momentum and energy will determine the resultant swirl, concentration and temperature of the fluid in the outer region, which is the source of the flow in the boundary

layer on the stator. Between the inner and outer regions, fluid leaves the boundary layer on the stator to be entrained by that on the rotor. Consequently, if the fluid is fully mixed in the outer region, the concentration of the fluid in the boundary layer on the stator, and that in the adjacent core, will be invariant with radius.

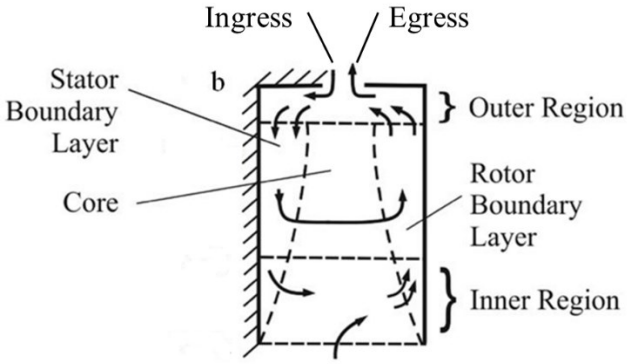

Figure 3: Simplified flow structure for a rotor-stator system with superposed sealing flow and ingress

Engine designers need to know: 1) how much sealing air is required to prevent ingress; 2) when ingress occurs, how much ingested fluid enters the wheel-space; and 3) what is the effect of ingress on the flow structure in the wheel-space. This paper describes the use of a three-dimensional, steady-state computational fluid dynamics (CFD) model to investigate ingress through two engine-representative turbine rim seals. The computations are validated using experiments conducted at the University of Bath; Scobie *et al.*[4] presented data which showed little effect of the rotor blades on the pressure downstream the vanes, suggesting this rig was suitable for steady CFD codes. The next section discusses previous CFD research associated with ingress in gas turbines. The experimental test facility used to validate the computations is then described. The computational model, the results and finally the conclusions are then presented.

Review of computational fluid dynamics related to ingress

There is a growing trend in industry to use complex 3D unsteady CFD codes to design rim seals and explore the mechanisms of ingress. Wang *et al.*[5] carried out 360 degree, time-dependent numerical simulations of a complete turbine stage with a rim seal and cavity. The results showed complex pressure

patterns which resulted from interactions between the blade and vane, while providing insight into the irregular circumferential pressure distribution known to be the driving force for ingress. Wang *et al*.[5] showed that the circumferential distribution of velocity of the ingress through the rim seal did not have a periodicity associated with either the blade or vane exit pressure variations.

Jakoby *et al*.[6] carried out unsteady simulations and identified energetic, large-scale flow structures which perturbed the pressure in the wheel-space at low sealing flow rates and increased ingestion levels. Increasing the sealing flow rate was found to dissipate these large-scale flow structures; these findings have been supported by recent unsteady computations by Julien *et al*.[7] and Dunn *et al*.[8].

Laskowski *et al*.[9] performed both steady and unsteady computations for ingress. Their computed results showed a difference in the contours of effectiveness between the two approaches. The steady results showed that while ingress occurred in the rim seal, it did not necessarily penetrate into the wheel-space; these results differed from the time-averaged unsteady results under similar conditions.

An alternative study involving Unsteady Reynolds-Averaged Navier-Stokes (URANS) computations and Large Eddy Simulations (LES) on rim-seal ingress was carried out by O'Mahoney *et al*.[10]. The results of both simulations were compared to experimental data, and it was found that the LES results gave better predictions (when compared to the measured sealing effectiveness) however, at the expense of much larger computational cost.

The experimental facility at the University of Bath (described in the next section) has been used to validate both steady and unsteady CFD models. Three-dimensional unsteady CFD simulations were carried out by Zhou *et al.*[11] for a simple axial-clearance seal, using a sector model with a single stator vane and rotor blade. To determine the sealing effectiveness, this model employed the solution of a transport equation for a passive scalar variable to represent the seeded tracer gas used in the experiments. Zhou *et al.*[11] confirmed, using unsteady computations, that the magnitude of the peak-to-trough pressure difference in the annulus is

the principal driving mechanism for ingress. Teuber *et al.*[12] carried out URANS computations for two-different rim seal geometries based on the same experimental rig. Two different pitch ratio models were tested: a 1:1 sector model (corresponding to 32 vanes and 32 blades) and a 4:5 model (corresponding to 32 vanes and 40 blades), that better represented the pitch variation in the experimental rig. The two models returned a virtually identical pressure distribution and non-dimensional pressure coefficient in the annulus, indicating that the (1/32) sector model was able to produce the correct annulus pressure variations to drive ingress at reduced computational cost. Teuber *et al*.[12] also computed swirl ratios and sealing effectiveness distributions in the wheel-space that matched experiments reasonably well over a range of sealing flow rates for both an axial and radial-clearance seal.

Rabs *et al.*[13] modelled the University of Bath rig using a steady frozen rotor approach, which fixed the rotor blade at a given position. It was found that the relative position of the blade with respect to the vane had a strong effect on the computed ingress. The frozen rotor approach was able to successfully compute the asymmetric pressure distribution in the annulus (where it was measured just downstream from the vane trailing edge); however, the measured radial distributions of effectiveness on the stator were not fully reproduced by computations for any of the fixed blade positions.

In this paper, 3D steady-state CFD has been carried out for a single and double clearance seal, without a rotor blade. This approach would be limited for situations where the annulus pressure asymmetry is strongly dependent upon the rotor. However, Scobie *et al.*[4] have presented experimental data in the test rig at Bath which showed little effect of the rotor blades on the pressure distribution downstream of the vanes. The steady-CFD approach has its limitations but provides insight into the fluid-dynamics of ingress at significantly reduced computational effort in comparison to the more complex unsteady codes used by engine designers.

Experimental test facility at the University of Bath

This paper makes use of the measurements of Sangan *et al.*[4, 14-16], who conducted extensive experimental research related to hot gas ingress into the wheel-space of a simplified axial turbine stage. The test section of the facility, shown in Figure 4, features a turbine stage with 32 stator vanes and 41 symmetric NACA 0018 section rotor blades. These unloaded blades eliminated the need for a dynamometer.

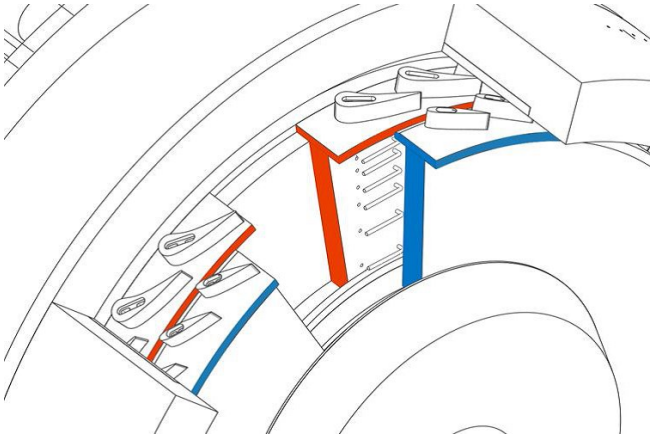

Figure 4: Rig test section highlighting pressure instrumentation (red, stationary; blue, rotating)

The disc could be rotated to a maximum speed of 4000 rpm, giving a maximum rotational Reynolds number, Re_ϕ (based on disc radius) of 1.1 x 10^6. This value is an order of magnitude less than that typically involved in gas turbines. However, for flows in rotating disc systems, the flow structure is controlled by the turbulent flow parameter, λ_T, and depends only weakly on Re_ϕ^2; therefore the flow structure in the test rig is believed to be representative of the wheel-spaces found in engines.

The vanes and blades in the annulus also produced a flow structure representative of that found in engines, albeit at lower Reynolds and Mach numbers. All experimental data for EI ingress presented in this paper is for the design condition listed in Table 1, where the flow coefficient and hence $Re_\phi / Re_W = 0.538$. The circumferential variation of static pressure in the annulus was determined from 15 taps in the vane platform arranged across one vane pitch[14]. At design conditions, with constant flow coefficient, the measured pressure distributions were independent of Re_ϕ for $M < 0.45$.

Table 1: Parameters for experimental EI ingress data at Bath Rig

Parameter	Disc Speed (RPM)
	3000
Re_ϕ	8.17 x 10^5
Re_W	4.4 x 10^5
Re_W / Re_ϕ	0.538
M	0.339

Sealing air was introduced into the wheel-space at a low radius. The sealing flow was seeded with a carbon dioxide (CO_2) tracer gas in order to measure the amount of ingestion. Concentration measurements were used to determine the *concentration effectiveness* ε_c. This is defined as

$$\varepsilon_c = \frac{c_s - c_a}{c_o - c_a} \qquad (1)$$

where the subscripts a, o and s respectively denote the air in the annulus, the sealing air at inlet, and at the surface of the stator. For the experiments, c_a and c_o were constants (approximately 0% and 1% respectively) and c_s varied with radius on the stator. In particular, $\varepsilon_c = 1$ when $c_s = c_o$ (zero ingress) and $\varepsilon_c = 0$ when $c_s = c_a$ (zero sealing flow). The concentration measurements were made within a combined uncertainty of +/- 0.015 %CO_2; a detailed uncertainty analysis is presented in Appendix 2.

The radial variation of concentration on the stator in the wheel-space, c_s, was measured by sampling through 15 tubes ($0.55 < r/b < 0.993$). The same taps were used to make measurements of the static pressure, p, on the stator. Seven complimentary pitot tubes, aligned with the tangential direction and at $z/S = 0.25$, were used to measure the total pressure p_T in the rotating core of fluid in the wheel-space. The tangential component of velocity in the core at each of the seven radial locations was calculated from Bernoulli's equation:

$$V_\phi = \left[\frac{2(p_T - p)}{\rho}\right]^{1/2} \qquad (2)$$

The estimated uncertainty in the measurements of V_ϕ were +/- 3% of the measured value.

A single seal configuration and a double seal configuration have been investigated in this paper, as illustrated in Figure 5. Experimental data for these seals has been previously published by Sangan *et al.*[15]. The notation used in this paper is S1 for the single seal and D1 for the double seal, which has the same outer rim seal geometry as S1. Further geometric details are shown in Figure 5.

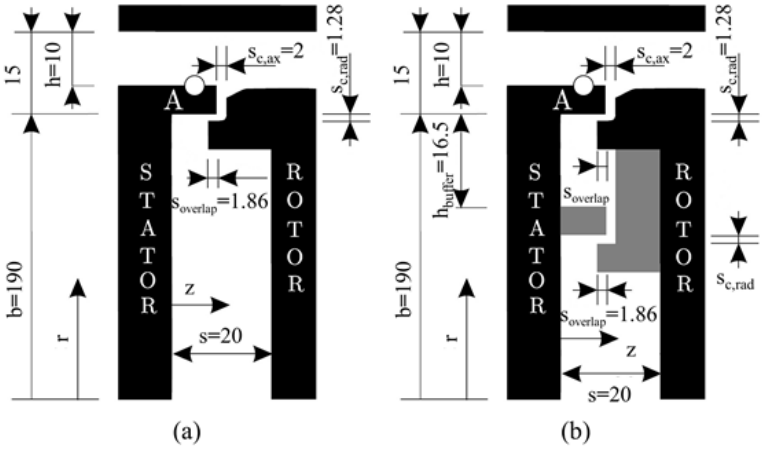

Figure 5: Rim-seal configurations investigated with geometric dimensions (mm); (a) Single seal, S1; (b) Double seal. D1

Computational Model

The commercial software package ANSYS CFX v13 was used for this investigation for continuity with the previous study of Teuber *et al.*[12]. The geometry (not to scale) and boundary conditions are shown in Figure 6, with two interfaces used between the three different model domains; the first Frame Change Interface (FCI) connects a stationary domain (stator) to a rotating domain (wheel-space), taking into account the change in frame reference, while the second General Grid Interface (GGI) connects the wheel-space to the rotor domain. The model geometry (including that of the stator vane) is based on the experimental test rig described above. For simplicity and for the other reasons discussed above, a geometry corresponding to 32 vanes and no blades has been used. The geometry of the rotating and stationary surfaces in the mainstream annulus and wheel-space is directly taken from the experimental rig. Figure 6 shows the geometry of the rim seal region and the wheel-space. A mass flow-rate boundary setting was applied at the mainstream and wheel-space inlets, with the sealing air seeded (using an additional passive scalar) to simulate the CO_2 tracer gas and

with no initial swirl. A fixed average static pressure condition was used at the outlet, and smooth wall settings were made for all solid surfaces.

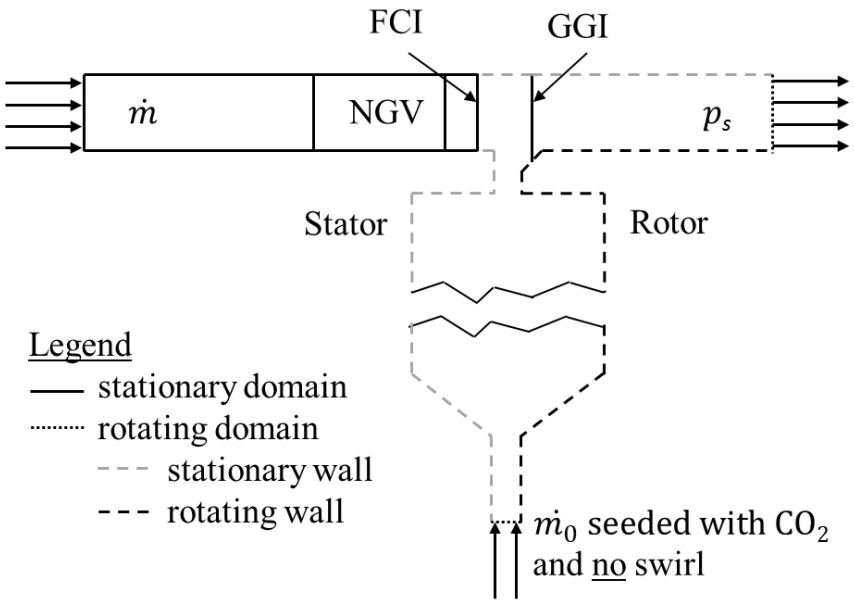

Figure 6: 1/32 sector CFD model with boundary conditions

The annulus height is 10 mm. The wheel-space gap between the rotor and stator is 20 mm, the axial clearance portion of the seal is 2 mm and the wheel-space outer radius is 190 mm. Further geometric properties of the various seal clearances are given in Figure 5.

ICEM v13 was used to generate the computational grid shown in Figure 7. The grid contained only hexahedral cells, using a j-grid topology for the stator domain (for which computations used a stationary frame of reference). This modelling approach does not involve a rotating blade in the rotor domain, reducing the mesh size significantly for the domain. The wheel-space was computed in the rotating frame of reference, with the frame-change interface (FCI) positioned between the stator and wheel-space domains as shown in Figure 6. The mesh contained 70 cells in the circumferential direction and 35 cells radially in the mainstream annulus. The two different rim seal computational models studied in this paper contain approximately 2.06 million nodes and 1.97 million hexahedral elements.

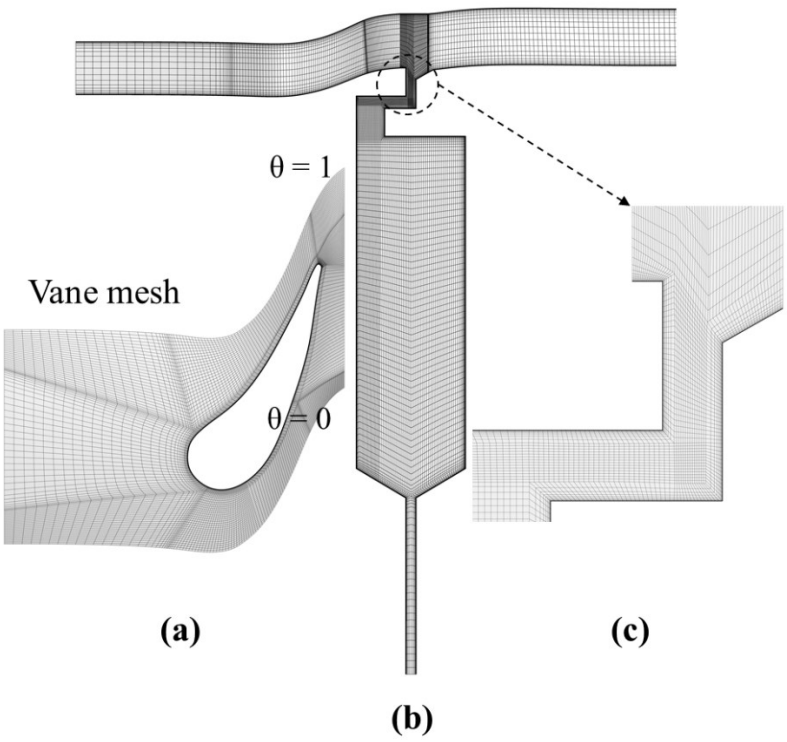

Figure 7: (a) Stator domain mesh with NGV; (b) Full model mesh shown in axial-radial plane (left, stator; right, rotor); (c) Seal gap region mesh

Mesh independence checks (covering a range of 0.5 million to 3.2 million nodes in total, due to the restrictions on computing facilities available) were carried out for the annulus pressure distribution downstream of the vane trailing edge and for the radial distribution of effectiveness in the wheel-space. Values of y^+ were less than 1 for the rotor, stator and wheel-space domains. The change in volume between adjacent cells was less than 10.

The steady RANS equations and the Shear-Stress-Transport (SST) turbulence model were used for the computations. The SST model offers a good compromise between accuracy and computing cost (Menter *et al.*[17]). The use of the SST turbulence model for ingestion computations is supported by the findings of Zhou *et al.*[11], Rabs *et al.*[13] and Teuber *et al.*[12].

The computations were conducted using two different settings, the Upwind Differencing Scheme and High Resolution Scheme. This was carried out to check whether the fluid dynamics, hence velocity profiles, within the rotor-stator wheel-space were influenced by the advection scheme. Figure 8 presents a comparison of a previous non-axisymmetric rotor-stator study against an experimental study by Chen *et al.*[18], which compared the predictive capabilities of the steady model and the effect of the advection scheme. The fluid dynamics in the wheel-space were found to be insensitive to the advection scheme, therefore a 1st order upwind difference scheme was used since it provided a robust method to compute ingestion at various different values of sealing flow rate. Another point to be noted is that the convergence level achieved by the Upwind Differencing Scheme is better than that of the High Resolution Scheme. An additional transport equation for a passive scalar was solved to simulate the CO_2 seeding of the sealing flow used in the experiments to obtain values of concentration effectiveness.

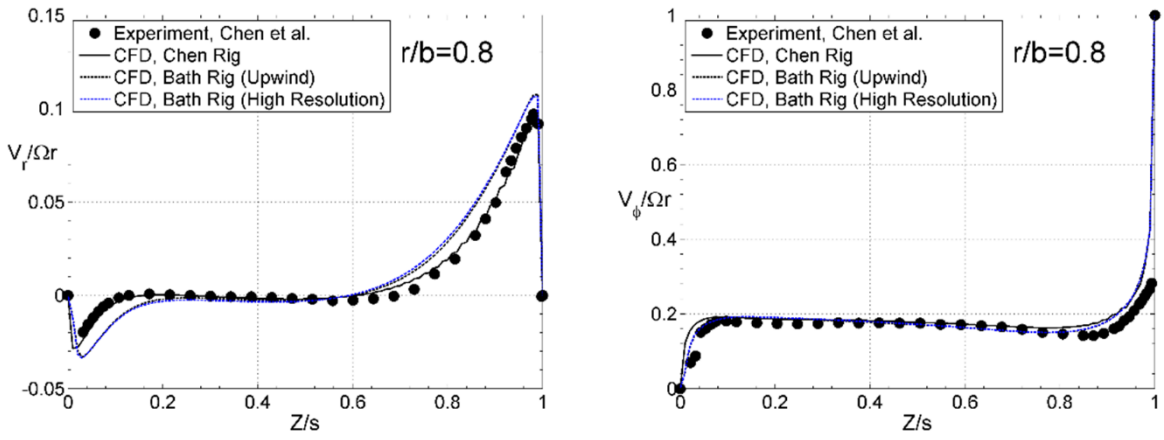

Figure 8: Comparison of velocity profiles for experimentally measured data and computed CFD models for the Chen Rig and Bath Rig (upwind and high resolution advection schemes) for $\lambda_T = 0.081$ at $Re_\phi = 1.25 \times 10^6$

The 3D steady computations were carried out using an eight CPU node of an HPC cluster at the University of Bath. Each computation required between around 24 to 48 hours depending on the magnitude of the sealing flow rate in the case being studied.

Convergence

The steady-state solutions were considered to be converged when residuals fell below the value of 10^{-4} of the maximum RMS (Root Mean Square) residuals for each variable and the monitored values of pressure, velocity and the additional transport equation reached steady values. The flow in the wheel-space was found to converge much more slowly than the flow in the annulus, due to the different timescales for the flow behaviour in these regions.

Convergence was affected significantly by the magnitude of the sealing flow rate. It was found that the model converged more quickly in computed cases where the wheel-space was nearly sealed from ingestion. It was possible to speed up the computations by increasing the (relaxation) time step of the additional transport equation by an order of magnitude compared to the conservation equations. Convergence rates were also influenced by the rim seal geometry being considered. The single seal was found to converge at approximately 10^{-4} for the maximum RMS residuals, compared to approximately 10^{-6} for the double seal.

CFD Validation

This section presents comparisons made between computational and experimental results, at a rotational Reynolds number of $Re_\phi = 8.2 \times 10^5$, for both the single and double seal illustrated in Figure 5. The present computations reproduce both the magnitudes and the trends of measured results for the flow in the annulus and in the wheel-space, and these are similar to time-averaged results obtained in other studies at greatly increased computational cost[12, 19].

Single Seal (S1)

Pressure Distribution in the Annulus

Figure 9 illustrates location A in the annulus (on the stator hub, 2.5 mm downstream of the vane trailing edge) where measured circumferential pressure distributions were determined experimentally. The data is shown as a non-dimensional pressure, C_p,

$$C_p = \frac{p - \bar{p}}{\frac{1}{2}\rho\Omega^2 b^2} \qquad (3)$$

where $\bar{p}$ is the mean static pressure in the annulus.

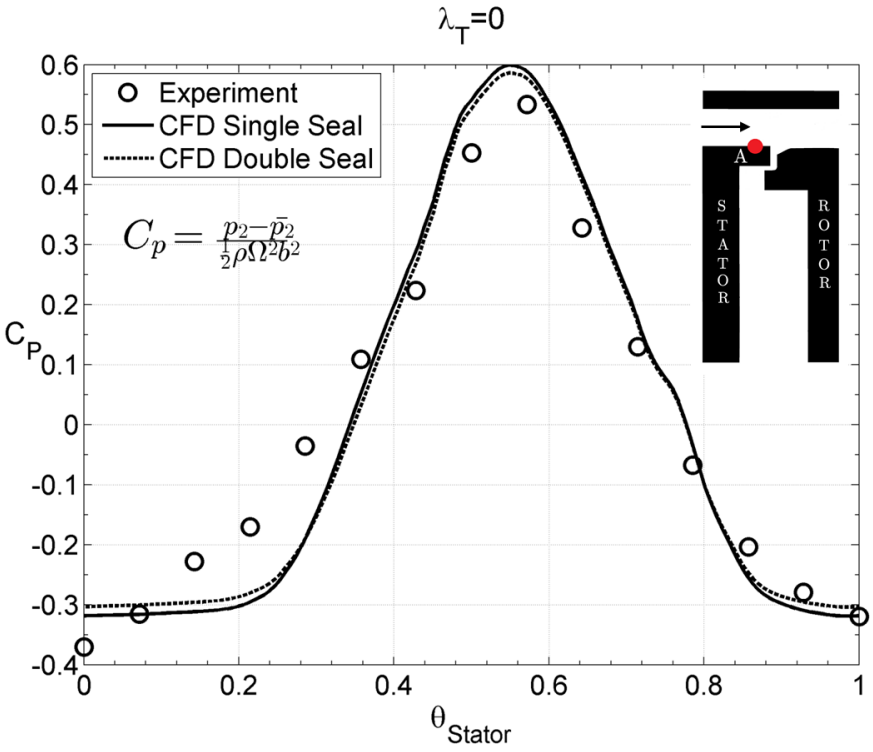

Figure 9: Comparison between measured and computed circumferential distribution of static-pressure in the annulus at location A (hub) at $Re_\phi = 8.2\text{x}10^5$

A comparison between the computed and measured distribution of the circumferential pressure distribution at location A for the case of no sealing flow (λ_T = 0) is shown in Figure 9. There is good qualitative agreement between the computations and the measured pressure distributions, although for 0.1 < θ < 0.4 there is an underprediction of measured C_p values of up to around 20% of the measured peak-to-trough circumferential variation. The computations over predict the measured maximum pressure; however the peak-to-trough pressure is similar to that in the experiments. This comparison shows that the computational model captures the primary driving mechanism for ingress, and that the blades appear to have only a small effect on the pressure distribution at this location.

Swirl Ratio in the Wheel-Space

Figure 10 illustrates the variation of swirl ratio with non-dimensional radius for the single seal (S1). The experimental measurement locations for total pressure in the wheel-space (at z/S = 0.25) are shown on the right of the figure in red symbols. The experiments and computations were carried out at Re_ϕ= 8.2 x10^5 for various values of λ_T. The symbols denote the experimental data, while the lines represent the computed swirl for the same conditions.

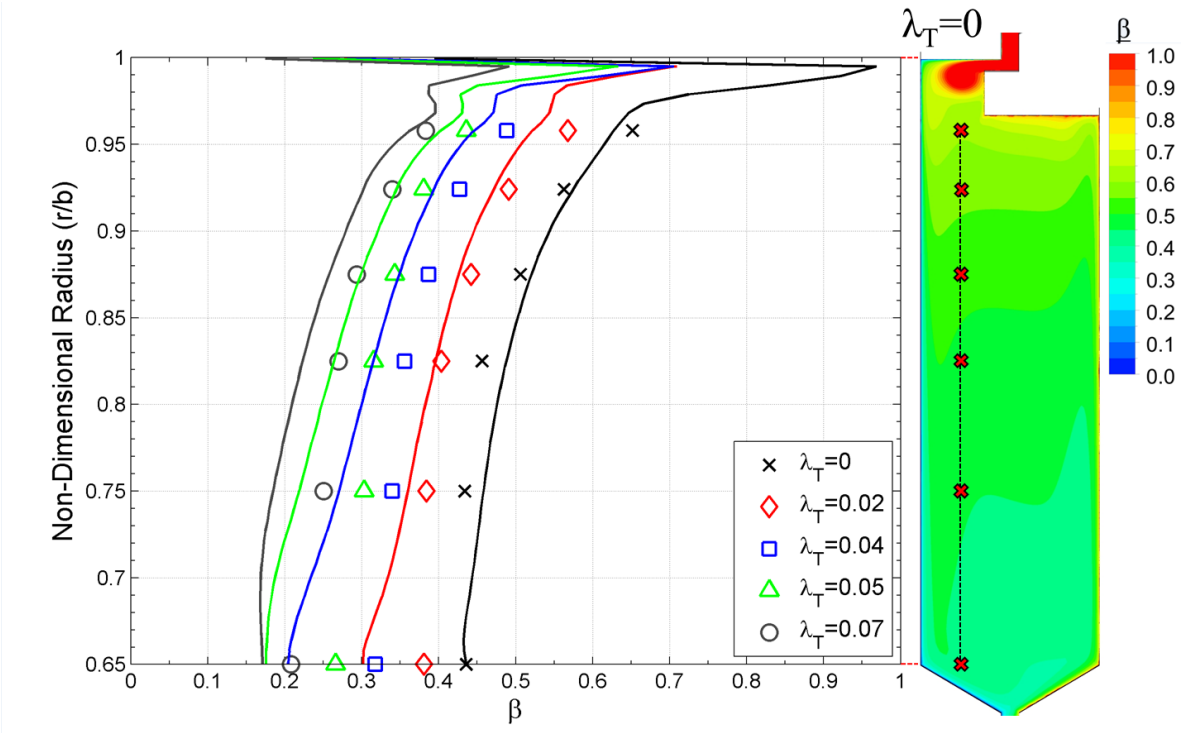

Figure 10: Variation of swirl ratio with radius for single seal for different λ_T at Re_ϕ = 8.2x10^5

The swirl distribution for the single seal S1 shows very good agreement between the computations and measurements, suggesting good prediction of the amount of ingestion and mixing of the fluid inside the wheel-space using the steady-state CFD model. The swirl distribution for λ_T = 0 is shown as a contour to the right of the plot. There is very good agreement for swirl ratio for r/b < 0.95; outward of this radius, where experimental data is not available, the swirl is observed to increase rapidly. The swirl in the annulus is β = 1.8.

Figure 10 shows that, as the sealing flow rate is increased, there is a reduction in the core rotation. The increased sealing flow rate pressurises the wheel-space; the swirl ratio near the periphery of the wheel-space also reduces, as the amount of ingress from the annulus reduces. The parametric variation of the swirl ratio with λ_T is well predicted by the computational model.

Sealing Effectiveness

Figure 11 shows the computed and measured radial variation of sealing effectiveness at the stator wall for three different sealing flow rates at Re_ϕ = 8.2 x 10^5. The symbols represent the experimental data, while the computations are represented by the lines. The computed results show good agreement with the experimental distribution for r/b < 0.9. The experimental data in Figure 11 illustrates that for all λ_T the effectiveness is broadly invariant with radius, suggesting that near-complete mixing has occurred in a region very close to the rim seal. However, at high radii, (0.9 < r/b < 1) the computations show a divergence from the measurements suggesting that the turbulence model and steady state simplifications do not capture fully the mixing process, which is inherently a complex unsteady phenomenon.

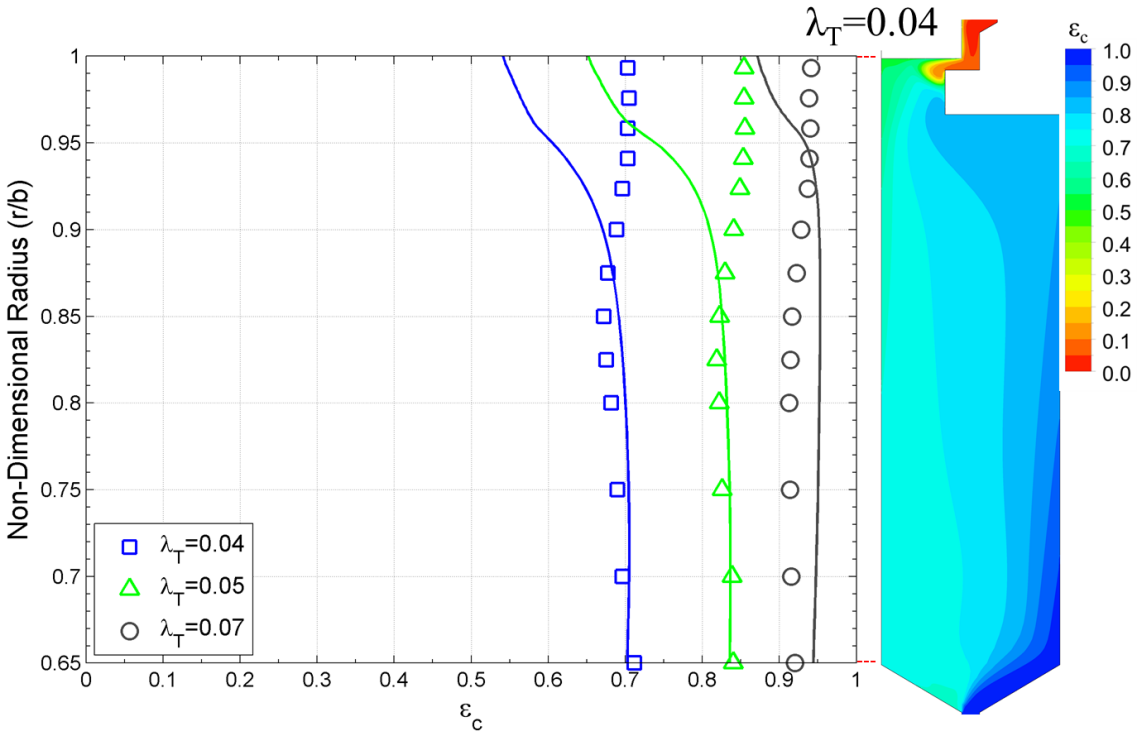

Figure 11: Effect of λ_T on radial variation of effectiveness for single seal at Re_ϕ = 8.2x10^5

Jakoby *et al.*[6], Teuber *et al.*[12] and Rabs *et al.*[13] all computed a radial variation of effectiveness which over-predicted measurements in the wheel-space; this (as discussed above) can probably be attributed to differences in behaviour in the mixing regions near the seal. The steady predictions shown here are better match to the experimental data than those obtained by Teuber *et al.*[12] (unsteady) and Rabs *et al.*[13] (frozen rotor).

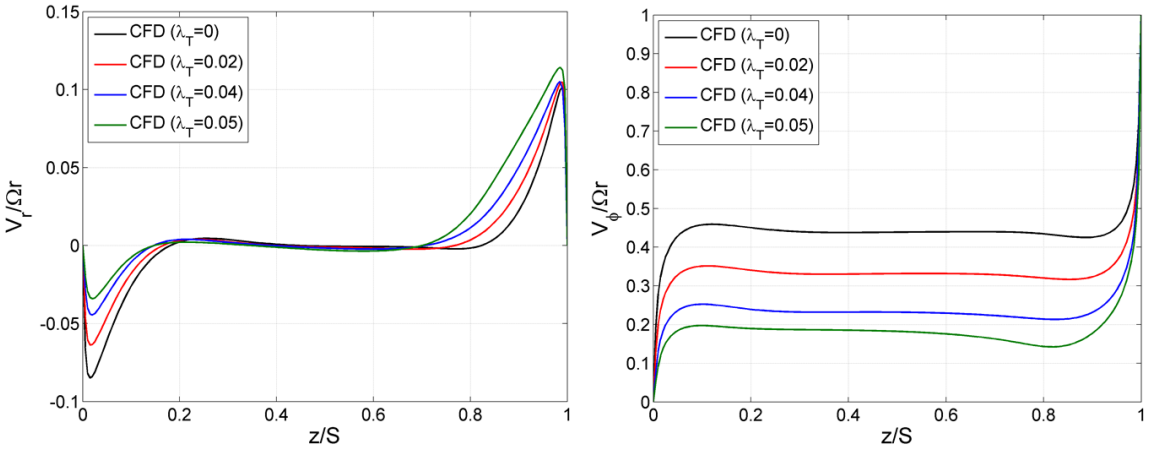

Figure 12: Computed velocity profiles at $r/b = 0.7$ for single seal for different λ_T at $Re_\phi = 8.2\text{x}10^5$

Figure 12 shows computed radial and tangential components of velocity for several λ_T, at $r/b = 0.7$ and for $Re_\phi = 8.2 \times 10^5$ for the single seal, S1. The flow structure is a turbulent version of that predicted for laminar flow between infinite disks by Batchelor[20]. There is radial inflow on the stator ($z/S = 0$), radial outflow on the rotor ($z/S = 1$), and between the boundary layers there is an inviscid rotating core in which $V_r = 0$ and $V_\phi / \Omega r \approx 0.44$ (for $\lambda_T = 0$). The effect of increasing the superposed flow is to reduce both the core rotation and the size of the boundary layer flowing inward on the stator, while increasing the flow moving radially outward on the rotor.

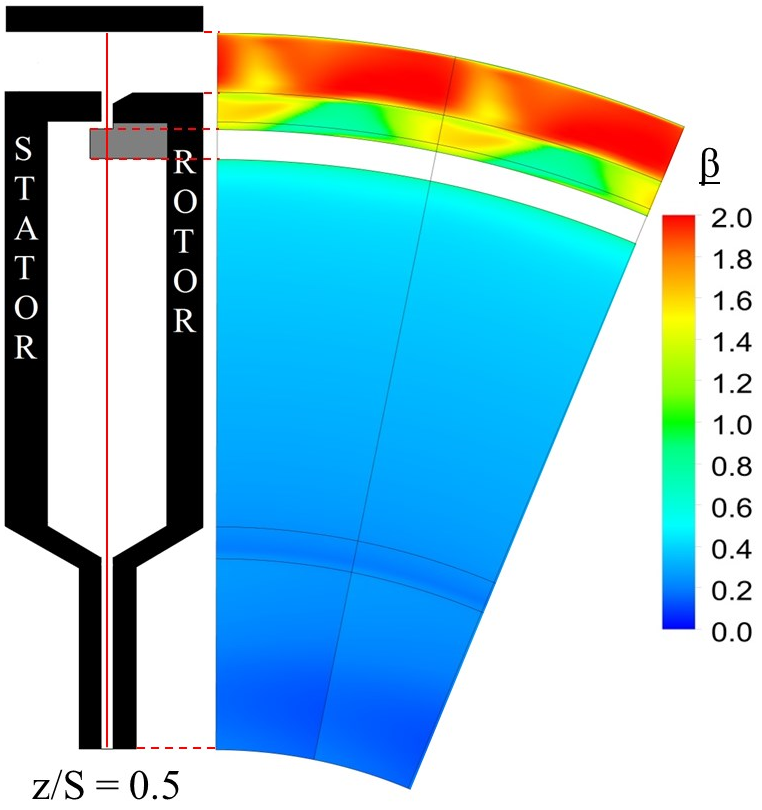

Figure 13: Swirl ratio at $z/S = 0.5$ for single seal at $\lambda_T = 0.04$

Figure 13 shows computed swirl ratio in the plane at $z/S = 0.5$ for seal S1 at $\lambda_T = 0.04$. The figure reveals that there is a non-axisymmetric swirl variation at high radius, which is attributed to the high swirl ingested fluid from the annulus. Comparisons of radial swirl variations are carried out by circumferentially averaging the computed data across the 11.25° sector model. Figure 14 shows concentration effectiveness on the stator and rotor surfaces for the same case. These computed results show that the mixing of the ingested fluid with the sealing flow takes place mainly within the seal-clearance and at high radius in the wheel-space; this explains the nearly uniform distribution of concentration effectiveness for $r/b < 0.9$ shown in Figure 11. At all radii, the effectiveness on the rotor is greater than that on the stator; this is the protective effect of the sealing flow in the rotor boundary layer, as illustrated in Figure 3.

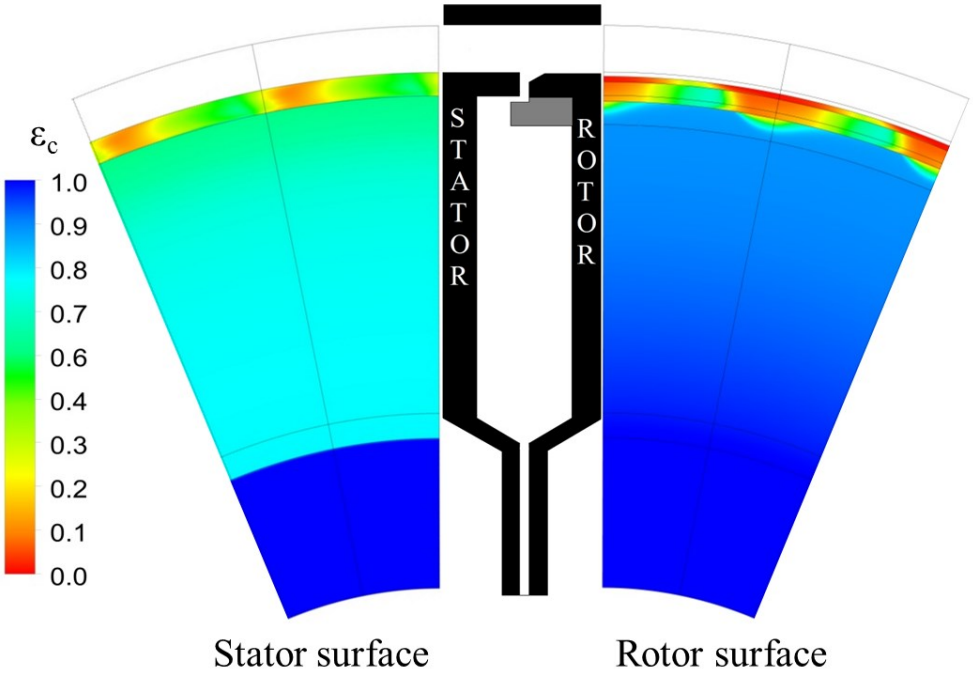

Figure 14: Concentration effectiveness on stator and rotor surfaces for single seal at $\lambda_T = 0.04$

Double Seal (D1)

Swirl Ratio in the Wheel-Space

Computed values of swirl and concentration effectiveness for the double seal (D1) are compared with experimental data in Figures 15 and 16 respectively. The seal geometry and measurement locations are shown in the schematic on the right. Figure 15 shows the radial distribution of swirl ratio at $z/S = 0.25$ in the wheel-space for the double seal. The symbols denote the experimental data, while the lines represent the computed swirl for the same conditions. The computations match qualitatively the variation of swirl ratio with radius for different values of λ_T, although the magnitude of the swirl ratio is lower for the computations than for the measurements in both the outer and inner wheel-space. This is likely to be due to difficulties in predicting accurately the details of the mixing in the confined outer wheel-space. In the inner wheel-space, the trends in the measurements are reproduced by the computations and agreement with measurements generally improves as the sealing flow rate reduces.

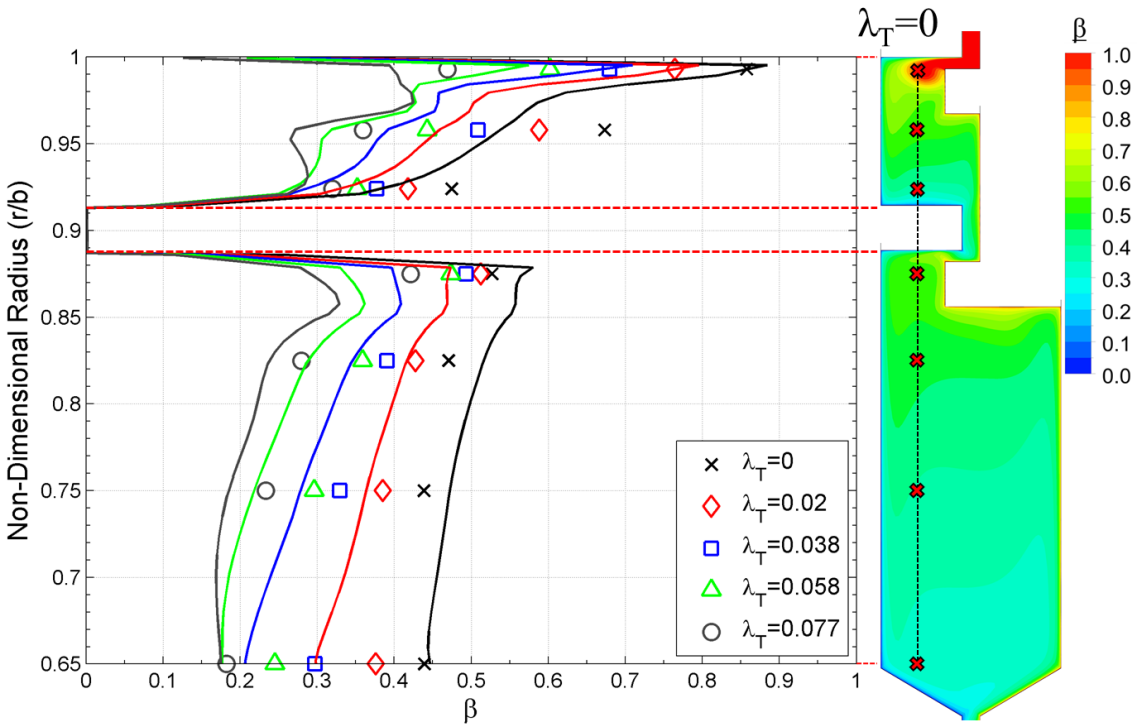

Figure 15: Variation of swirl ratio with radius for double seal for different λ_T at $Re_\phi = 8.2\text{x}10^5$

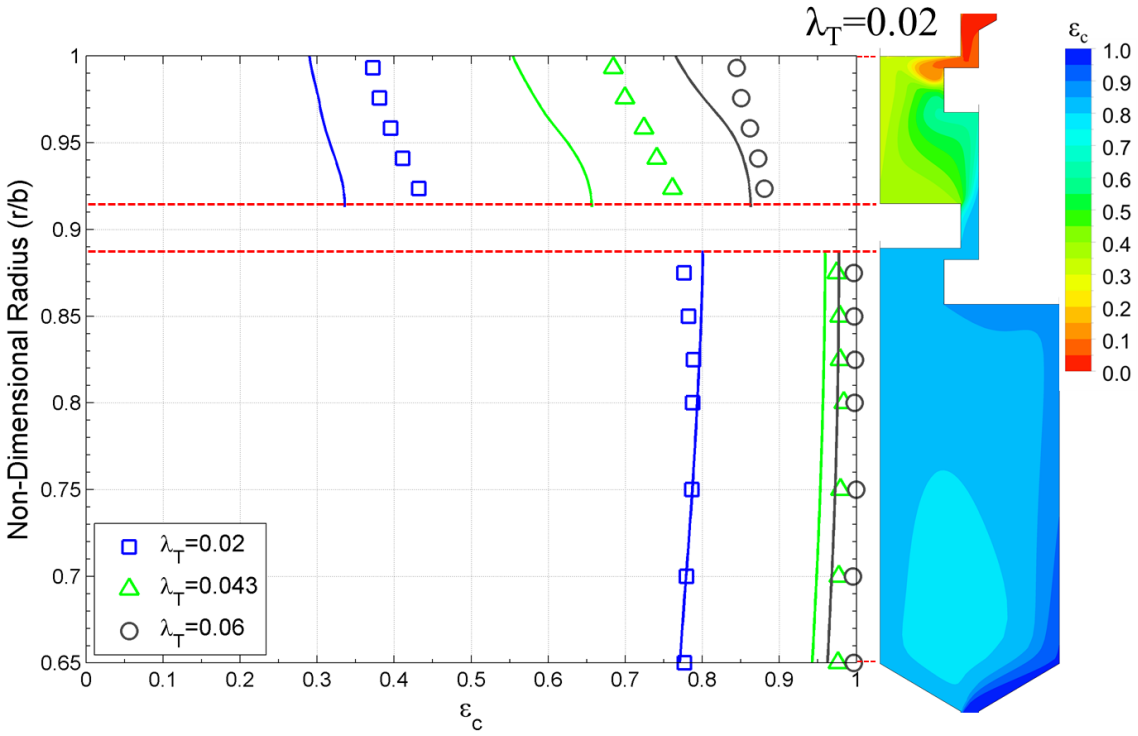

Figure 16: Effect of λ_T on radial variation of effectiveness for double seal at $Re_\phi = 8.2\text{x}10^5$

The data for the double seal for $\lambda_T = 0$ (Figure 15), show an almost invariant behaviour of swirl with radius inward of the inner seal ($r/b < 0.85$). In contrast, the swirl ratio is seen to increase considerably in the outer wheel-space ($r/b > 0.924$) under the influence of the fluid with high swirl ingested from the annulus. For all cases, the computed swirl ratio in the outer wheel-space is lower than that measured experimentally; however, the qualitative trend is predicted, and the sudden increase of swirl at $r/b \approx 0.875$ due to the rotating radial insert is captured. As described above, increasing the sealing flow rate (*i.e.* increasing λ_T) causes a reduction in the swirl ratio in the inner wheel-space for both the computed and experimental results. This is the case for both the single and double seal. The swirl ratio in the outer wheel-space also reduces as the ingress reduces. For all test cases, the difference between computation and experiment is less than 33% of the measured value. The differences are largest in the outer wheel-space, where the variation of swirl with radius is greatest. In the inner wheel-space, this difference is about 10% for the $\lambda_T = 0$ case. The difference between computations and experiments varies with sealing flow-rate and radial location.

Figure 16 shows the radial distribution of sealing effectiveness on the stator for the double seal. Experimental data is also included for comparison. Both computational results and experimental data show an increased sealing effectiveness in the inner wheel-space, with most of the high-swirling ingress constrained to the outer wheel-space. The computations reproduce qualitatively the trends in the measured sealing effectiveness in the outer wheel-space, but with under-prediction of the measurements which again suggests some deficiencies with this simplified model. The effectiveness in the inner wheel-space is in good agreement with the experimental data, predicting the effectiveness within about 5% of the measured value for all cases.

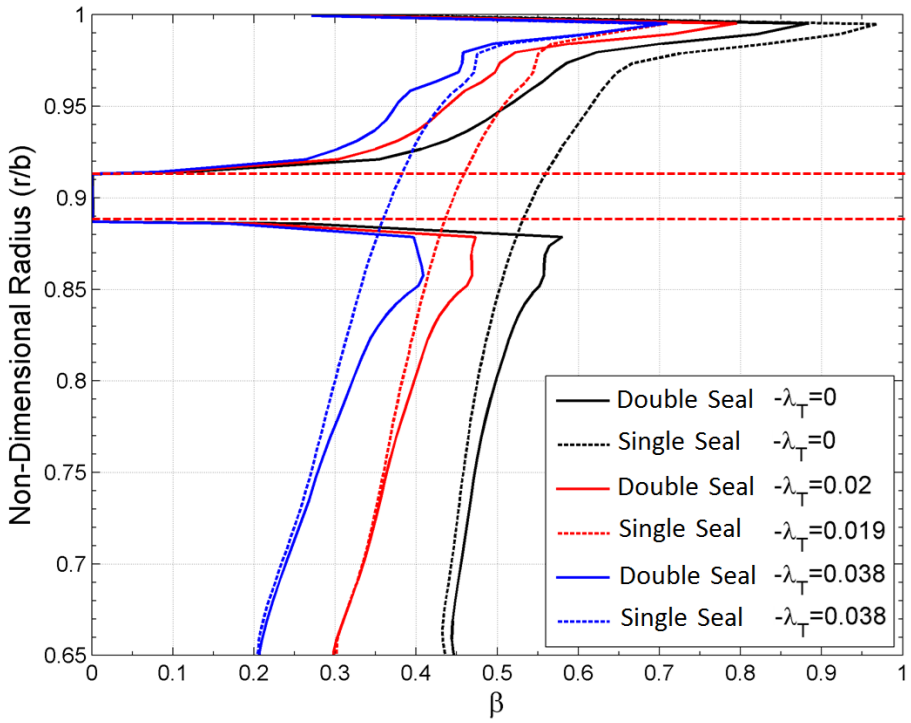

Figure 17: Comparison of computed variation of swirl ratio with radius between double seal and single seal for similar λ_T values at $Re_\phi = 8.2\times10^5$

Figure 17 presents a comparison between the double seal and the single seal for the swirl ratio distribution for similar λ_T. The swirl for both seals is similar but with two major differences identified. Firstly the double seal experiences a lower swirl in the outer wheel-space than the single seal for similar λ_T; this can be explained as the double seal has a smaller volume (due to the radial inserts), thus requiring less sealing flow to pressurise the wheel-space, hence reducing ingress. Secondly, the swirl at $r/b \approx 0.875$ for the double seal is influenced by the lower section of the rotating inner radial seal. As shown in Figures 11 and 16, there are significant differences in the ingress into the wheel-space for the two seals. Despite this, differences in the measured swirl only appear near the outer periphery and the flow structure is governed principally by λ_T.

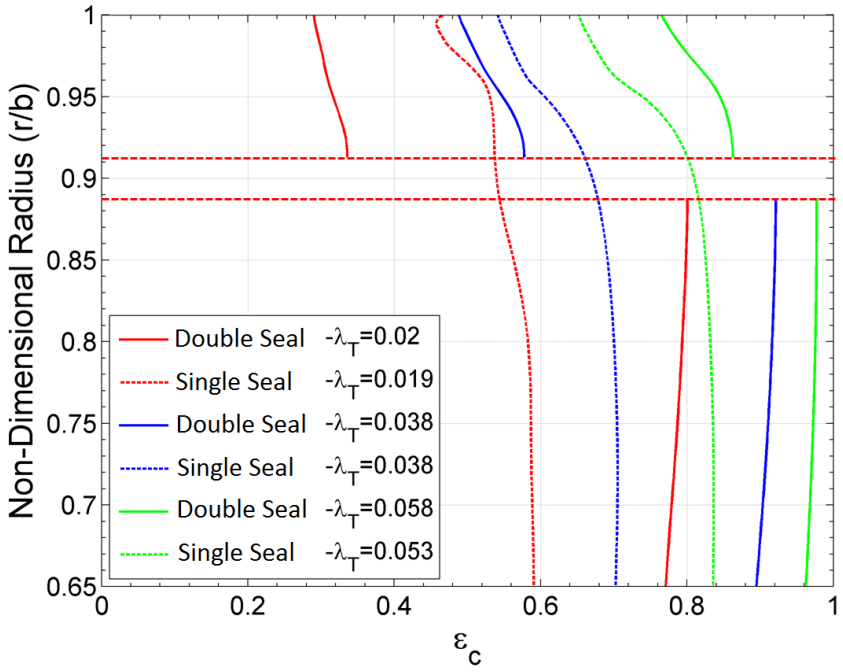

Figure 18: Comparison of computed variation of effectiveness with radius between double seal and single seal for similar λ_T values at $Re_\phi = 8.2\times10^5$

Figure 18 presents a comparison of the radial distribution of effectiveness between the double seal and the single seal. The effectiveness for the double seal radially inward of the inner seal is significantly higher than those for the single seal at the same sealing flow rate. The effectiveness is virtually constant for $0.65 < r/b < 0.875$. The outer wheel-space ($r/b > 0.924$) shows a significant decrease in effectiveness as ingested fluid is largely contained in the space between the two seals. The reduction of effectiveness with increasing radius in this region indicates that the flow in the outer wheel-space has not fully mixed.

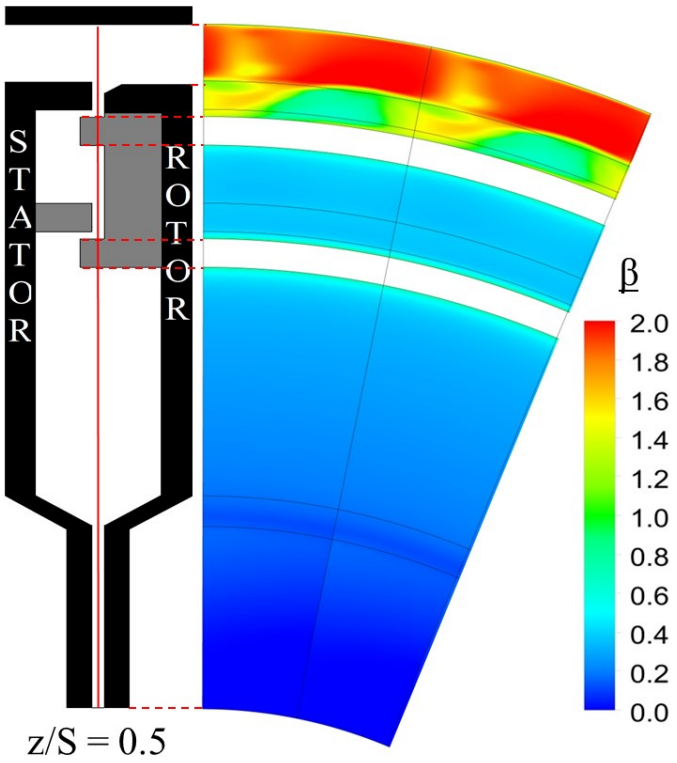

Figure 19: Swirl ratio at $z/S = 0.5$ for double seal at $\lambda_T = 0.04$

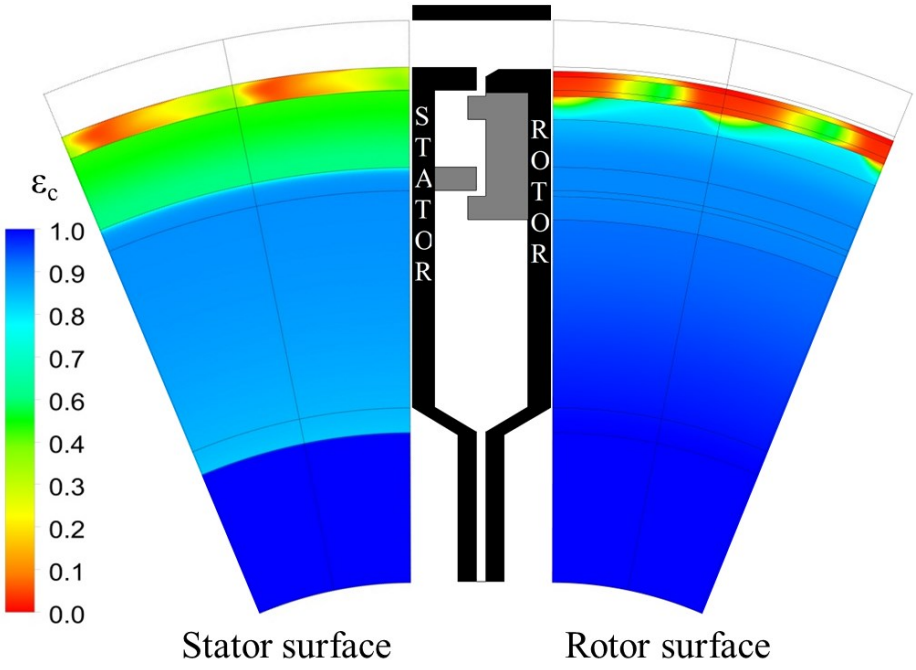

Figure 201: Concentration effectiveness on stator and rotor surfaces for double seal at $\lambda_T = 0.04$

Figure 19 shows the computed swirl ratio in the plane at $z/S = 0.5$ for seal D1 at $\lambda_T = 0.04$ (similar to Figure 13). Highly swirling flow is ingested from the annulus into the wheel-space, increasing the swirl at high radii. Figure 20 displays the concentration effectiveness on the stator and rotor surfaces for the same case. The figure again clearly illustrates the improved sealing performance of the double seal for the inner wheel-space region compared with the single seal results shown in Figure 14. Figure 20 also shows that the ingested fluid is confined in the outer wheel-space where some mixing still takes place, with fully mixed fluid in the inner wheel-space indicated by the uniform concentration shown in Figure 16 at $r/b < 0.875$. The protective effect of the rotor boundary layer is also observed.

Conclusions

The commercial computational fluid dynamics code CFX v13 has been used to carry out RANS computations to investigate the fluid dynamics of ingress for two different engine-representative rim-seal geometries in a 3D model of a turbine stage, without the rotating blades.

The computations reproduce the main features of the measured asymmetric pressure distribution in the annulus caused by the stationary vanes, where the peak-to-trough pressure variation is the driving force for ingress through rim seals in engines. Determining the annulus pressure variation required significantly less computational effort that the corresponding computations of ingress into the wheel-space. There is good agreement between the computed and measured trends for swirl ratios in the wheel-space, indicating that ingress is predicted well by RANS computations for the geometry and conditions studied here. The greatest differences between computed and measured swirl ratios are around 33% of measured values; the differences vary with swirl ratio and sealing flow-rate. The present results are similar to time-averaged results obtained in other studies at greatly increased computational cost. The steady-state approach to modelling a 3D turbine stage used here is an alternative to traditional unsteady CFD codes which can take up to several weeks (or months) of computational time. The computational results have provided insight to the mechanisms of ingress and how this ingested fluid affects the flow structure within the wheel-space.

Acknowledgments

The computations were carried out using an eight CPU node of the Aquila HPC cluster at the University of Bath. This research received no specific grant from any funding agency in the public, commercial, or not-for-profit sectors.

References

1. Sangan CM, Pountney OJ, Zhou K, Wilson M, Owen JM and Lock GD. "Experimental Measurements of Ingestion through Turbine Rim Seals-Part 2: Rotationally Induced Ingress," *ASME J Turbomach* 2013; 135(2). 021013 (formerly ASME paper GT2011-45313).
2. Owen JM and Rogers RH. *Flow and Heat Transfer in Rotating-Disc Systems*. vol. 1, Rotor stator systems. Taunton, UK: Research Studies Press Ltd, 1989.
3. Childs PRN. *Rotating Flow*. Oxford: Butterworth-Heinemann, 2010.
4. Scobie JA, Sangan CM, Teuber R, Pountney OJ, Owen JM, Wilson M and Lock GD. "Experimental Measurements of Ingestion through Turbine Rim Seals. Part 4: Off-Design Conditions," ASME Paper GT2013-94147, 2013.
5. Wang CZ, Johnson BV, Mathiyalagan SP, Glahn JA and Cloud DF. "Rim Seal Ingestion in a Turbine Stage from 360-Degree Time-Dependent Numerical Simulations," ASME Paper GT2012-68193, 2012.
6. Jakoby R, Zierer T, Devito L, Lindblad K, Larsson J, Bohn DE, Funcke J and Decker A. "Numerical simulation of the unsteady flow field in an axial gas turbine rim seal configuration," ASME paper GT2004-53829, 2004.
7. Julien S, Lefrancois J, Dumas G, Boutet-Blais G, Lapointe S and Caron JF. "Simulations of flow ingestion and related structures in a turbine disk cavity," ASME paper GT2010-22729, 2010.
8. Dunn DM, Zhou DW, Saha K, Squires KD, Roy RP, Kim YW and Moon HK. "Flow field in a single-stage model air turbine rotor-stator cavity with pre-swirled purge flow," ASME paper GT2010-22869, 2010.
9. Laskowski GM, Bunker RS, Bailey JC, Ledezma G, Kapetanovic S, Itzel GM, Sullivan MA and Farrell TR. "An investigation of turbine wheelspace cooling flow interactions with a transonic hot gas path – Part 2: CFD simulations," *ASME J Turbomach* 2011; 133(4). 041020 (formerly ASME paper GT-2009-59193).

10. O'Mahoney TSD, Hills NJ, Chew JW and Scanlon T. "Large-eddy simulation of rim seal ingestion," ASME paper GT2010-22962, 2010.

11. Zhou K, Wilson M, Owen JM and Lock GD. "Computation of Ingestion through Gas Turbine Rim Seals," *Proceeding of the Institution of Mechanical Engineers. Part G, Journal of Aerospace Engineering* 2013; vol. 227(7), pp.1101-1113.

12. Teuber R, Li YS, Maltson J, Wilson M, Lock GD and Owen JM. "Computational extrapolation of turbine sealing effectiveness from test rig to engine conditions," *Proceedings of the Institution of Mechanical Engineers, Part A: Journal of Power and Energy* 2013; vol. 227(2), pp. 167-178.

13. Rabs M, Benra FK, Dohmen HJ, Lock GD and Schneider O. "Model simplifications for numerical simulation of ingestion through gas turbine rim seals," In: *ISROMAC-14*, Honolulu, HI, 27 February–2 March 2012.

14. Sangan CM, Pountney OJ, Zhou K, Wilson M, Owen JM and Lock GD. "Experimental Measurements of Ingestion Through Turbine Rim Seals-Part 1: Externally Induced Ingres," *ASME J Turbomach* 2013; 135(2). 021012 (formerly ASME paper GT2011-45310).

15. Sangan CM, Pountney OJ, Scobie JA, Wilson M, Owen JM and Lock GD. "Experimental Measurements of Ingestion through Turbine Rim Seals. Part 3: Single and Double Seals," 2013, *ASME J. Turbomach 2013* 135(5), 051011 (formerly ASME Paper GT2012-68493).

16. Sangan CM, Lalwani Y, Owen JM and Lock GD. "Experimental Measurements of Ingestion through Turbine Rim Seals. Part 5: Fluid Dynamics of Wheel-Space," ASME Paper GT2013-94148, 2013.

17. Menter FR, Kuntz M and Langtry R. "Ten years of industrial experience with the SST turbulence model," In: K Hanjalic, Y Nagano and M Tummers (eds) *Turbulence, heat and mass transfer*, 4. New York: Begell House, 2003, pp.625–632.

18. Chen JX, Gan X, and Owen JM. "Heat Transfer in an Air-Cooled Rotor–Stator System," 1996, *ASME J. Turbomach 1996* 118(3).

19. Teuber, R., 2014, "Computation of Rim-Seal Ingestion for Gas Turbines", PhD Thesis, University of Bath.

20. Batchelor GK. "Note on a class of solutions of the Navier-Stokes equations representing steady rotationally-symmetric flow," *Quart. J. Mech. Appl. Maths*, 1951, 4, pp. 29-41.

Appendix 1:

Notation

b	radius of seal
c	concentration
C_p	pressure coefficient ($= (p_2 - \bar{p}_2) / ({}^1/_2\, \rho\Omega^2 b^2)$)
$C_{w,o}$	nondimensional sealing flow rate ($=\dot{m}_o/\mu b$)
G_c	seal-clearance ratio ($=s_c/b$)
h	annulus height
$\dot{m}_o$	mass flow rate
p	absolute static pressure
$\bar{p}$	mean absolute static pressure over one vane pitch
r	radius
Re_W	axial Reynolds number in annulus ($=\rho W b/\mu$)
Re_ϕ	rotational Reynolds number ($=\rho\Omega b^2/\mu$)
S	axial gap between rotor and stator in wheel-space
$s_{c,ax}$	axial seal clearance
$s_{c,rad}$	radial seal clearance
u_t	friction velocity ($=(\tau_w/\rho)^{1/2}$)
U	bulk mean radial velocity component of sealing air through the seal clearance
V_r, V_ϕ	radial and tangential components of velocity
W	axial velocity in annulus
y	distance of near-wall node from wall surface
y^+	nondimensional wall distance ($=yu_t\rho/\mu$)
z	axial distance from the stator

β	swirl ratio ($=V_\phi/\Omega r$)
ε	sealing effectiveness ($=c_s/c_o$)
λ_T	turbulent flow parameter ($= C_{w,o}Re_\phi^{-0.8}$)
μ	dynamic viscosity
θ	normalized tangential coordinate across one vane
ρ	density
τ_w	wall shear stress
Ω	angular speed of rotating disc
FCI	Frame Change Interface
GGI	General Grid Interface

Subscripts

a	annulus
e	egress
EI	externally-induced (ingress)
i	ingress
max,min	maximum, minimum
s	value on stator
o	sealing flow

Appendix 2:

Uncertainty in effectiveness measurements

For convenience, the definition of sealing effectiveness (ε_c denoted here for simplicity as ε) given in eq (1) is repeated below:

$$\varepsilon = \frac{c_s - c_a}{c_o - c_a} \qquad (4)$$

where the subscripts a, o and s respectively denote the air in the annulus, the sealing air at inlet, and the surface of the stator.

Let $\delta_\varepsilon, \delta_s, \delta_o, \delta_a$ be uncertainties in $\varepsilon, c_s, c_o, c_a$ respectively so that

$$\begin{aligned}\varepsilon \pm \delta_\varepsilon &= \frac{c_s \pm \delta_s - (c_a \pm \delta_a)}{c_o \pm \delta_o - (c_a \pm \delta_a)} \\ &= \frac{(c_s - c_a)[1 + (\pm\delta_s \pm \delta_a)/(c_s - c_a)]}{(c_o - c_a)[1 + (\pm\delta_o \pm \delta_a)/(c_o - c_a)]}\end{aligned} \qquad (5)$$

$$= \varepsilon \frac{[1 + (\pm\delta_s \pm \delta_a)/(c_s - c_a)]}{[1 + (\pm\delta_o \pm \delta_a)/(c_o - c_a)]} \qquad (6)$$

If $(\pm\delta_o \pm \delta_a)/(c_o - c_a) \ll 1$ then

$$\varepsilon + |\delta_\varepsilon| \le \varepsilon \left\{ 1 + \frac{|\delta_s| + |\delta_a|}{c_s - c_a} + \frac{|\delta_o| + |\delta_a|}{c_o - c_a} \right\} \qquad (7)$$

Hence,

$$\frac{|\delta_\varepsilon|}{\varepsilon} \le \left\{ \frac{|\delta_s| + |\delta_a|}{c_s - c_a} + \frac{|\delta_o| + |\delta_a|}{c_o - c_a} \right\} \qquad (8)$$

If the uncertainty is a percentage of the full-scale range, which was the case in the experiments, then $\delta_s = \delta_o = \delta_a = \delta$, say, and eq (8) simplifies to

$$\frac{|\delta_\varepsilon|}{\varepsilon} \le 2\delta \frac{1 + \varepsilon^{-1}}{c_o - c_a} \qquad (9)$$

or

$$|\delta_\varepsilon| \le 2\delta \frac{1 + \varepsilon}{c_o - c_a} \qquad (10)$$

The average standard deviation, σ, in the range $0 < \varepsilon < 1$ can be calculated from eq (10) by

$$\sigma = \frac{2\delta}{c_o - c_a} \sqrt{\int_0^1 (1 + \varepsilon)^2 d\varepsilon} = 3.06 \frac{\delta}{c_o - c_a} \qquad (11)$$

The CO_2 gas analyser had an overall uncertainty of 1½% of each of its ranges. In the tests, where the 1% range was used, the concentration of gas in the sealing flow was close to the 1% range maximum. Hence $\delta/(c_o - c_a) \approx 0.015$ %CO_2, and from eq (11) it follows that $\sigma \approx 0.046$.